



This work was carried out in whole or in part within the framework of the NOMATEN Center of Excellence, supported from the European Union Horizon 2020 research and innovation programme (Grant Agreement No. 857470), the European Regional Development Fund via the Foundation for Polish Science International Research Agenda PLUS programme (Grant No. MAB PLUS/2018/8), *and the initiative of the Ministry of Science and Higher Education 'Support for the activities of Centers of Excellence established in Poland under the Horizon 2020 program' under agreement No. MEiN/2023/DIR/3795.*

This is the accepted manuscript submitted to: *Archiv.Civ.Mech.Eng* 24, 76 (2024), published on 13 March 2024 with the embargo period till: 13 March 2025.

DOI: 10.1007/s43452-024-00889-7

Effect of SPS consolidation and heat treatment on microstructure and mechanical behavior of FeCrAl-Y₂O₃ ODS alloys with different Ti and V contents

Tomasz Stasiak^{1,*}, Jarosław J. Jasiński^{1,2}, Łukasz Kurpaska^{1,2}, Wojciech Chmurzyński¹, Marcin Chmielewski^{1,3}, Magdalena Wilczopolska², Katarzyna Mulewska^{1,2}, Maciej Zieliński², Hanna Purzyńska⁴, Michał Kubecki⁴, Marcin Kowal¹, Jacek Jagielski^{1,2}

¹National Centre for Nuclear Research, Materials Research Laboratory, A. Sołtana 7 St., 05-400 Otwock-Świerk, Poland;

²National Centre for Nuclear Research, NOMATEN Centre of Excellence, A. Sołtana 7 St., 05-400 Otwock-Świerk, Poland;

³Lukasiewicz Research Network, Institute of Microelectronics and Photonics, Wólczyńska 133 St., 01-919 Warsaw, Poland

⁴Lukasiewicz Research Network - Institute for Ferrous Metallurgy, K. Miarki 12-14 St., 44-100 Gliwice, Poland

* Corresponding author: Tomasz Stasiak

tomasz.stasiak@ncbj.gov.pl

National Centre for Nuclear Research, Materials Research Laboratory, A. Sołtana 7 St., 05-400 Otwock-Świerk, Poland

Phone number: +48 510443296

Abstract

Oxide dispersion strengthened (ODS) alloys, due to their high irradiation resistance and good mechanical properties at high temperatures, are promising for applications in Generation IV reactors, especially GFR, and fusion installations. However, the biggest challenge in applying ODS materials is related to fabrication techniques. This paper aims to evaluate powder metallurgy processing and the effect of small additions of oxide and carbide-forming elements on the microstructure and mechanical properties of FeCrAl-based ODS alloys. The series of ODS alloys with Y₂O₃ and different additions of Ti and V was prepared by mechanical alloying (MA) and consolidated by spark plasma sintering (SPS), which is less often employed to fabricate ODS alloys than hot extrusion or hot isostatic pressing. The investigations were performed on MAed powders, bulk-sintered samples, and samples after homogenization annealing. The MAed powders reveal two body-centered cubic (bcc) alloyed phases with close lattice parameters. The sintered samples show a single bcc phase ($a = 2.88\text{-}2.89 \text{ \AA}$) matrix and a high-volume fraction of homogeneously distributed nanometric oxide precipitates. The addition of vanadium and titanium leads to the formation of vanadium and titanium-rich nanometric oxides and carbides. The bulk samples show fine grain and stable microstructure with an average grain size slightly below 1 μm . Moreover, after homogenization annealing and air cooling, the relative density slightly increases. Hardness after heat treatment is relatively stable, which was confirmed by nanoindentation and Vickers microhardness results. These experimental findings promise to develop FeCrAl-based ODS materials tailored for operation under harsh conditions in nuclear reactors.

Keywords: ODS alloy, powder metallurgy, mechanical alloying, spark plasma sintering, microstructure characterization

1. Introduction

The nuclear power industry is a near-zero carbon dioxide emission energy source in fast development, especially connected with the implementation of Generation IV nuclear reactors, which present significantly better fuel efficiency, minimized proliferation risk, and higher safety standards [1]. However, one of the biggest problems in these installations is that materials should operate under extreme conditions, i.e., intensive radiation (up to 150-200 dpa) and high temperatures up to 1000°C [2]. Such environment requires structurally stable materials and resistant to creep (thermo-mechanical loads) conditions. In this case, one of the solutions could be the application of Fe-Cr-Al-based oxide dispersion strengthened (ODS) alloys, which show great potential as materials for high-temperature nuclear applications, including under creep conditions [3]. These materials could be applied for, e.g., Accident Tolerant Fuel (ATF) claddings [4], or steam generator components in the next-generation super-critical water-cooled reactor (according to the review by Rahman et al. [5] or studies by Isselin et al. [6]) and boiling water reactors [7]. Moreover, FeCrAl ferritic alloys, with varying chromium and aluminum contents, have also been extensively studied for nuclear components used in next-generation reactors, e.g., GFR/HTR technology (hot gas ducts, heat removal elements) applications [2]. It is due to their superior oxidation and corrosion resistance mainly driven by the passive alumina (α -Al₂O₃) layer inherent to the bulk material formed during high-temperature operation [8].

Moreover, these ferritic alloys, having a bcc structure as opposed to the Ni-stabilized fcc structure of austenitic Fe-based alloys, and thus exhibit better stress corrosion cracking (SCC) resistance. [9] However, FeCrAl alloys have a limited long-term operating temperature (~800°C) [10], which hinders their use due to the formation α (with high iron content) and α' (with high chromium content) phases and so-called 475°C embrittlement effect [11]. It is worth mentioning that compositions with less Cr should be less prone to thermal aging and embrittlement. [11] Moreover, precise steering with Al addition also significantly affects the α - α' phase separation effect. [12] In addition, Al contributes to the stabilization of ferrite in alloys with less than 12 wt. % of Cr [13] and improves oxidation resistance; however, yield strength and creep resistance still require improvement. Therefore, a promising approach is the modification of the microstructure and chemical composition of the FeCrAl alloy with oxide particles and carbide-forming elements. Wang et al. [14] revealed the possibility of the fabrication of FeCrAl ODS with Y₂O₃, Zr, and W additions, which show good mechanical properties and homogeneously distributed different nanometric oxides. Another recent study by Yang et al. [15] showed the formation of different types of oxides in FeCrAl-Y₂O₃-Ti-Zr alloy, which can improve the strength of the alloy. Massey et al. [16] found the appearance of (Y, Al, O)-rich high-density nanoprecipitates of 2-4 nm in diameter in FeCrAl-ODS alloy.

In this paper, we continue our work [17] on FeCrAl-based alloys with additions of yttrium oxide (Y₂O₃), titanium, and vanadium up to 0.3 wt.%, 1 wt.%, and 0.5 wt.%, respectively. These additions improve the properties thanks to the ability to form nanometric complex oxides and carbides, e.g., according to Oksiuta et al. [18], the addition of vanadium could lead to an

increase in hardness due to nanoprecipitates rich in vanadium. Moreover, such composed microstructure of FeCrAl ODS alloys is characterized by fine bcc grains and homogeneously distributed nanometric oxides, hindering grain boundary migration and pinning dislocations reducing their motions at high-temperature conditions [19]. Nanoprecipitates can act as sinks for point defects generated during radiation exposure [20] and prevent thermal aging embrittlement [21]. So far, ODS Fe-Cr alloys have been studied with many promising results, e.g., Frelek-Kozak et al. [22], who studied ODS alloy with 12% Cr, revealed the possibility of obtaining material that shows good ion irradiation resistance and consists of fine matrix and homogeneously distributed nanoprecipitates, while Zhang et al. [23] showed promising results of Fe-14Cr-0.4Ti-0.25Y₂O₃ ferritic ODS alloy. It should be noted that the type of oxide in ODS alloys has an important effect on irradiation resistance [24].

However, FeCrAl-based ODS modified with yttria, titanium, and vanadium are less studied, particularly regarding the impact of manufacturing methods and appropriate selection of heat treatment processes. The most common manufacturing technique for ODS alloys is powder metallurgy, involving mechanical alloying (MA) and consolidation with hot isostatic pressing (HIP) [25], hot extrusion (HE) [26], or spark plasma sintering (SPS), e.g., studies by García-Rodríguez et al. [27] or investigations by Macía et al. [28]. The mechanical alloying process offers advantages such as extended solubility of elements, absence of element segregation, and compatibility with alloys containing elements with significantly different melting temperatures [29]. Notably, mechanical alloying yields fine-grained structures that also positively impact the mechanical properties of the bulk material [30]. As mentioned, methods such as HIP (e.g., [31]) and HE (e.g., [32]) are commonly known for bulk ODS alloys production, while SPS is still an emerging technique. which can produce microstructures with equiaxed grains and minimal texture [33]. Furthermore, short heating times in SPS enable nearly full densification and the formation of complex nano-sized oxides, thus preventing coarse microstructure and excessive grain growth [23]. However, diffusion during short-time SPS sintering is limited, underscoring the importance of chemical homogeneity achieved during mechanical alloying [22]. Thus, post-sintering thermal processing, such as homogenization annealing, might also impact the properties of ODS alloys. This paper investigates the feasibility of manufacturing FeCrAl-based ODS alloys enriched with Y₂O₃, Ti, and V using SPS consolidation and controlled heat treatment (homogenization annealing).

The study primarily focuses on the role of Y₂O₃ oxide particles and Ti and V addition on microstructure homogeneity and hardness of the FeCrAl-based ODS alloys after annealing at 1020°C. Although still in the preliminary research stage, the study has yet yielded promising results, prompting authors to present initial characterization and findings.

2. Materials and methods

2.1. Materials and processing techniques

In this study, eight compositions of FeCrAl ODS alloys are selected (Table 1). Iron is the base element in all studied alloys. The content of Al is fixed at 5%, while the content of Y₂O₃ is fixed at 0.3% in all investigated samples. Al is supposed to improve oxidation resistance by forming a protective layer on the surface. Y₂O₃ oxide is selected as a strengthening phase because it shows a high melting point, high chemical stability, and low solubility in the metal

matrix. The amount of Y_2O_3 was selected based on the literature data. The content of Cr, which is a ferrite stabilizer, is either 9 or 12%. Slight differences in Cr or Al could significantly impact “475°C embrittlement” related to the alpha and alpha prime separation. S. Kobayashi et al. [11], who studied FeCrAl alloys with different Cr and Al contents, found out that the addition of Al can suppress the “475°C embrittlement” in the FeCrAl alloys containing more than 12% of Cr. The studies of FeCrAl alloys by W. Han et al. [12] revealed that appropriately balancing Cr and Al content can limit “475°C embrittlement”. The authors plan to investigate resistance to “475°C embrittlement” in detail later. The content of Ti is either 0.5 or 1%. The small addition of Ti can improve the corrosion resistance of the alloys, which will be studied later in detail. Moreover, the high affinity of Ti towards oxygen could lead to the formation of nanometric oxide precipitates. A small amount of V (0.5%) is added to selected samples. Vanadium could also form nanometric oxide precipitates, and its high affinity to carbon could result in carbide formation. Therefore, the additions of Ti and V could improve the mechanical properties of the FeCrAl ODS alloys.

Table 1. Chemical composition of FeCrAl- Y_2O_3 -Ti-V ODS alloys selected for mechanical alloying and spark plasma sintering.

Sample	Chemical composition [wt.%]					
	Fe	Cr	Al	Y_2O_3	Ti	V
M1	Bal.	9	5	0.3	0.5	---
M2	Bal.	9	5	0.3	1.0	---
M3	Bal.	12	5	0.3	0.5	---
M4	Bal.	12	5	0.3	1.0	---
M5	Bal.	9	5	0.3	0.5	0.5
M6	Bal.	9	5	0.3	1.0	0.5
M7	Bal.	12	5	0.3	0.5	0.5
M8	Bal.	12	5	0.3	1.0	0.5

2.2. Processing techniques

The purity and particle size of commercially purchased powders from Alfa Aesar are listed in Table 2. The mechanical alloying (MA) was carried out in a Retsch PM100 planetary ball mill. All powder processing procedures before MA were conducted in a glove box under an argon atmosphere. Each milling batch produces about 50 g of powder. The balls and grinding jar material was X90CrMoV18 martensitic stainless steel, and the balls-to-powder ratio was 5:1. The mechanical alloying duration was 50 hours with 250 rpm, and a 15-minute break was applied after every 15 minutes to maintain mechanical alloying close to RT. The MA procedure was performed without the addition of a process control agent. Next, the mechanically alloyed powders were consolidated using the SPS technique in a device designed by the Lukasiewicz Institute of Microelectronics and Photonics. The SPS process was conducted in a graphite round die with a diameter of 25 mm with a heating rate of 100°C/min up to 900°C; then, the heating rate was lowered to 50°C/min until reaching the sintering temperature of 1050°C. The sintering temperature and uniaxial pressure of 40 MPa were kept for 10 minutes. Then, the samples were slowly cooled down (average cooling rate of 10°C/min). Then, the first campaign of bulk

materials investigation was realized, and subsequently, the bulk samples were heat treated at 1020°C for 30 min in a Nabertherm furnace under an argon atmosphere and cooled down in air.

Table 2. Purity and particle size of commercial powders used for FeCrAl-Y₂O₃-Ti-V ODS manufacturing.

Component	Fe	Cr	Al	Y ₂ O ₃	Ti	V
Purity	99.9% metal basis, C ≤ 0.2%, O ≤ 0.4%	99.99% metal basis, C < 10 ppm, O < 160 ppm	99.5% metal basis	99.9%, total rare earth oxide 0.1% max.	99.8% metal basis, C = 0.086%, O = 0.694%	99.5% metal basis, C ≤ 0.034% O ≤ 0.035%
Particle size	< 20 μm	<150 μm	< 30 μm	< 10 μm	< 70 μm	< 40 μm

2.3. Characterization techniques

The mechanically alloyed powders were studied by scanning electron microscopy (SEM) using a Zeiss EVO MA10 device equipped with an energy-dispersive X-ray spectroscopy (EDS) detector. Moreover, the phase investigation of the powders was carried out using the X-ray diffraction (XRD) technique. The XRD patterns were collected using a Bruker D8 Advance diffractometer. The density of bulk samples after sintering and after annealing was measured according to Archimedes' principle. Before the measurements, samples were polished using SiC abrasive papers (approximately 0.5 mm) to limit the effect of surface contamination by carbon from graphite die or oxidizing during heat treatment. The density measurements were performed by weighing the samples in air and distilled water at 23°C. The measured densities were then compared with the theoretical densities calculated based on the rule of mixtures using pure elements densities. The SEM-EDS and electron backscatter diffraction (EBSD) analyses of bulk samples were conducted using a ThermoFisher Scientific™ Helios™ 5 UX Scanning Electron Microscope equipped with an EDAX Elite Super Detector EDS system. The sample preparation for SEM-EDS and EBSD consisted of cutting slices of material from the central part of bulk samples and mechanical polishing using up to P1200 grit SiC abrasive papers. Subsequently, the samples were electropolished using a Struers Lectropol system with the following procedure: 60% perchloric acid 70 ml + ethanol 1000 ml, duration: 50 s, temperature: 10°C, voltage: 30 V. The grain analysis of the collected EBSD data was conducted by EDAX OIM Analysis 8 software. The sample preparation for the TEM and STEM-EDS analyses was carried out by focused ion beam (FIB) technique using a ThermoFisher Scientific™ Helios™ 5 UX. The TEM/STEM-EDS investigations were performed using a JEOL JEM 1200EX II TEM operating at 120 kV and a JEOL F200 operating at 200 kV equipped with two EDS detectors, allowing chemical composition investigations of nanometric precipitates. Based on STEM and TEM images, the size distribution and particle volume fraction analysis were realized using ImageJ software. The total area of images used for the calculations was approximately 5 μm². The sintered samples' carbon and oxygen content measurements were performed using CS-600 LECO and TCHEN600 LECO analyzers. The X-ray diffraction

(XRD) technique was used to investigate the phase structure of the prepared bulk samples. The diffraction patterns of bulk samples were acquired using a Bruker D8 Advance diffractometer with a Cu anode powered by 40 kV and 40 mA. The data was analyzed using a Bruker DIFFRAC.EVA (database ICDD PDF4+ 2022 [34]) and a DIFFRAC.TOPAS software. The Vickers microhardness measurements were conducted using a DuraVision hardness tester by Zwick/Roell under a load of 4.90 N. For each sample, ten measurements were performed after SPS and homogenization annealing. The nanoindentation measurements were carried out using a NanoTest Vantage System by Micro Materials Ltd. at ambient temperature with a Berkovich-shaped diamond indenter tip. The nanoindentation tests were conducted in a single-force mode by applying 11 different forces ranging from 0.5 mN to 10 mN. The measurements were repeated at each load 20 times with a 20 μm spacing between indents. Dwell time was fixed at 2 s. Loading and unloading time were set at 5 s and 3 s for lower loads (0.5-4 mN) and 10 s and 5 s, respectively, for higher loads (5-10 mN). The nanoindentation data was analyzed based on the load-displacement curves applying the Oliver and Pharr method [35].

3. Results and Discussion

3.1. Results of powder preparation and mechanical alloying

The SEM imaging of mechanically alloyed powders realized for samples M1-M8 demonstrates flattened particles with irregular shapes and rough surfaces, as illustrated in Figure 1. The morphological characteristics of the powders remain consistent between all studied chemical compositions. Particle size was also analyzed using SEM images, revealing a wide range of size distribution in all of the samples. Among these, fine particles with a diameter of a few micrometers coexist with agglomerates with size of more than 150 μm . However, the majority of particles are around 50 μm in size.

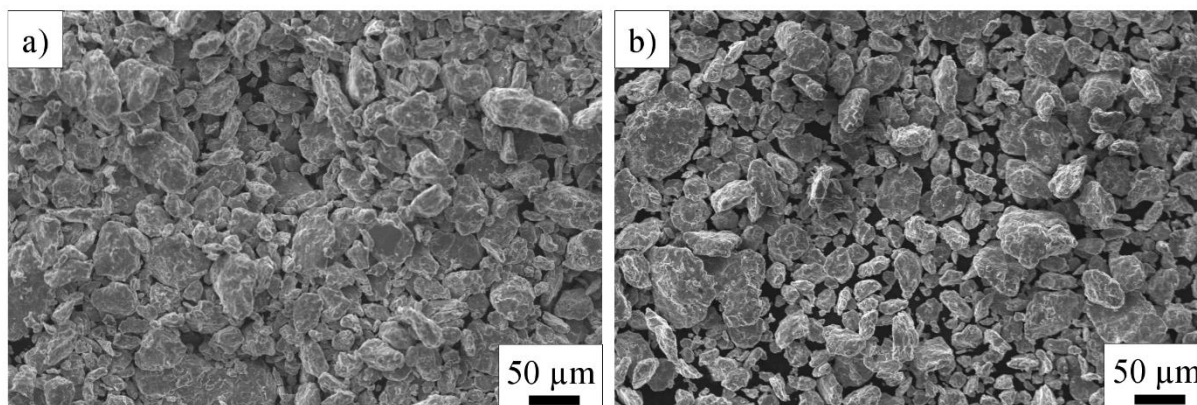


Fig. 1. SEM secondary electron images of selected mechanically alloyed powders acquired using the working distance of 10 mm and accelerating voltage of 20 kV: a) M1 sample and b) M6 sample.

Figure 2 presents SEM-EDS selected point analyses of the FeCrAl-Y₂O₃-Ti-V ODS powders' chemical composition, indicating the presence of all constituent elements within the mechanically alloyed powders. These outcomes affirm the appropriateness of the selected milling parameters in producing uniform powder particles during mechanical alloying.

Furthermore, no pure particles were found in the ground powders. It is also significant that no isolated Y_2O_3 particles are present; therefore, it can be expected that the oxide particles are dispersed uniformly within the grains and will be homogeneously distributed in the material after the consolidation process. The uniform distribution of nanometric precipitates is crucial for irradiation resistance. Thus, these precipitates act as sinks for irradiation-induced defects. The irradiation resistance will be studied in detail later.

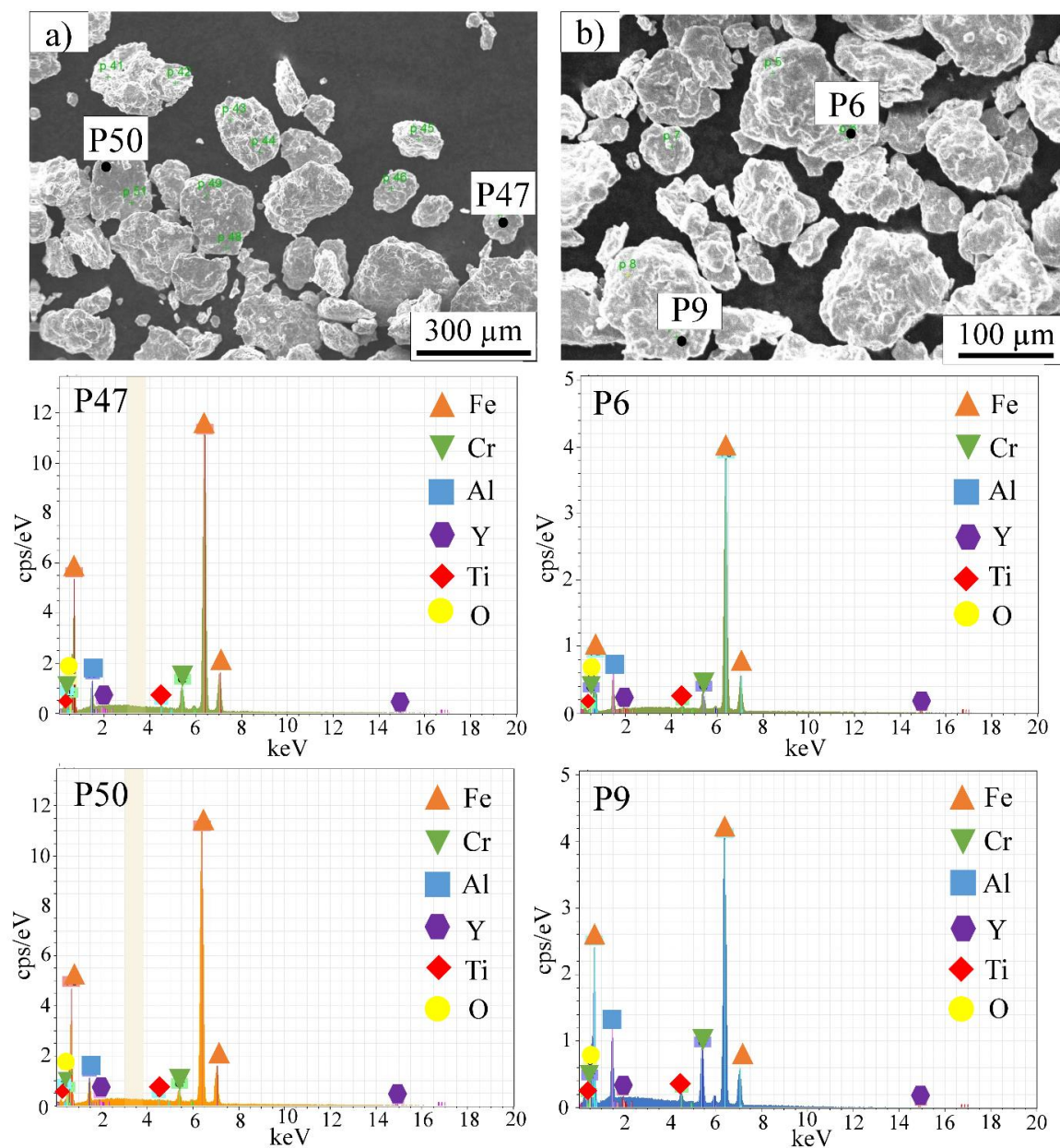


Fig. 2. SEM-EDS chemical composition analysis of FeCrAl- Y_2O_3 -Ti-V ODS FeCrAl ODS powders after mechanical alloying performed at the working distance of 10 mm and accelerating voltage of 20 kV: a) M2 and b) M3 sample.

The XRD results, shown in Fig. 3, reveal two bcc phases in all samples after mechanical alloying. It should be noted that the XRD patterns were acquired from 15° to 145° of 2θ .

However, between 15° and 35° , the background noise that originates mainly from the scattering of X-rays on air is more intense; therefore, the results for these angles are not shown after ensuring that no peaks are present between 15° and 35° of 2θ . The lattice parameter of the bcc1 phase is between 2.866 and 2.869 Å, which is close to the lattice parameter of pure Fe ($a = 2.866$ Å). The lattice parameter of the bcc2 phase is between 2.889 and 2.891 Å, which is close to the lattice parameter of pure Cr ($a = 2.885$ Å). Most studies of the Fe-Cr-Al systems report the formation of the bcc phase, i.e., S. Xu et al. [31] found a single bcc matrix phase in ODS samples with 9% of Cr and containing Al in the amount between 0.4 and 4.5%; C. Chen et al. [30] revealed the formation of a single bcc matrix phase in Fe-20Cr-5.5Al-0.5Ti-0.5Y₂O₃ ODS alloy prepared by powder metallurgy. Moreover, the phase diagram of the Fe-Cr-Al system predicts the formation of a single bcc phase, although it should be noted that the mechanical alloying is not an equilibrium process. However, the differences between the two phases are minor and thus related to the slight differences in chemical composition due to incomplete homogenization during mechanical alloying. The addition of Ti and V alloying elements does not seem to impact the formation of solid solution phases during mechanical alloying. It could be because the additions of these elements are minor, and thus, both components could easily dissolve in the primary bcc solid solutions. The volume fraction of Y₂O₃ and other oxides formed during mechanical alloying is too small to be detected by the XRD technique due to the limited sensitivity of this method. Crystallite size decreases significantly during mechanical alloying from 74 nm in pure Fe powder to 10-30 nm in the bcc phases in the powder after mechanical alloying.

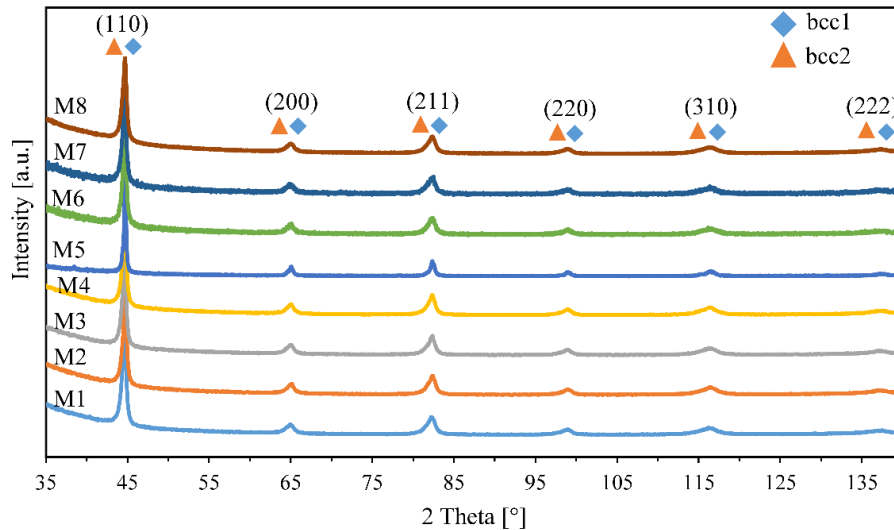


Fig. 3. XRD patterns of mechanically alloyed powders of FeCrAl-Y₂O₃-Ti-V ODS (samples M1-M8).

3.2. Bulk samples characterization – as-sintered and annealed

The results of density measurements using the Archimedes method reveal good densification of the material after SPS, i.e., the relative density between 95.5 and 96.1%, except the M1 sample, which shows slightly lower density (Fig. 4). The SPS method allows good densification of different metallic materials [36]. The density is comparable to the samples prepared in other

studies about ODS alloys, e.g., 97% investigated by Q.X. Sun et al. [37] or 96.3% relative density obtained by A. Mori et al. [38] in some samples, but it still seem lower than the densities (above 98%) presented in papers by M. Frelek-Kozak et al. [24] and N. García-Rodríguez et al. [27]. According to the literature, the relative density often increases rapidly with increasing sintering temperature [23]. However, it should be noted that the theoretical density values in this paper were calculated based on the density of pure elements using the rule of mixtures. Therefore, these theoretical calculations only account for 0.3% of Y_2O_3 without accounting for oxides that form during the mechanical alloying and sintering. The powder metallurgy processing often leads to oxygen contamination and the formation of additional oxides. The measured oxygen content in the investigated samples is quite high, e.g., 0.44 wt.% in the M4 sample or 0.42 wt.% in the M8 sample. The oxides, having a lower density than the bcc ferritic matrix phase, significantly impact the final density of the material. Moreover, the presence of carbide could also decrease the density. Carbon contamination was found in all samples, which is common for powder metallurgy-prepared samples. For example, the carbon content in the M8 sample is 0.078 wt.%. Therefore, the relative densities presented in this paper should be considered instead of absolute value rather as an indication to compare density among samples and could be used to compare the density after homogenization annealing. Moreover, it should be noted that the SEM observations do not show significant porosity, cracks, or structure discontinuities. The visible pores are small and homogeneously distributed. Therefore, the present porosity, which is difficult to avoid in the powder metallurgy manufactured samples, will have a relatively limited impact on mechanical properties. The homogenization annealing leads to a slight increase of relative density in all produced bulk samples (Fig. 4) by decreasing the porosity. The relative density increase is more pronounced in the M1-M4 samples, which are vanadium-free samples. The increase in the relative density is less visible in vanadium-containing samples (M5-M8). It could be due to the formation of additional vanadium-rich oxides and, eventually, carbides during homogenization annealing from the vanadium dissolved in the ferritic matrix. These precipitates can present lower density than the bcc matrix, and therefore, they can decrease overall density.

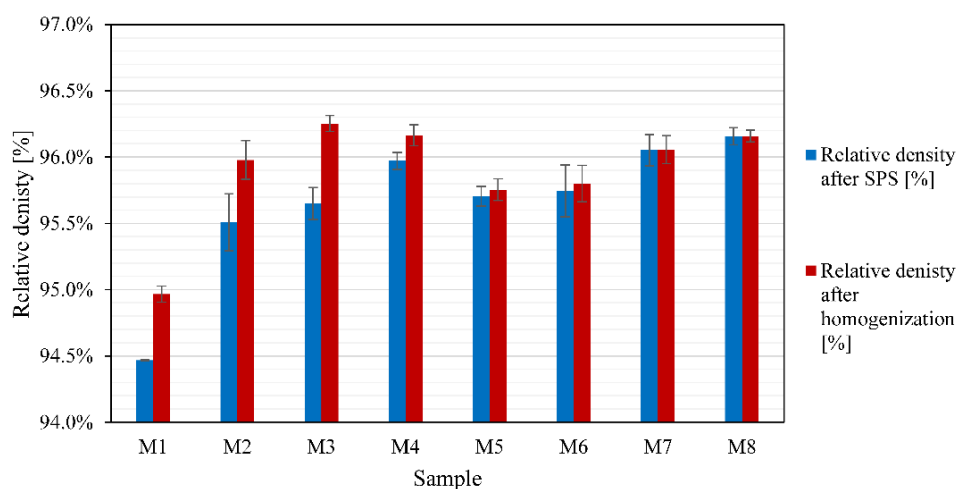


Fig. 4. Density of FeCrAl- Y_2O_3 -Ti-V ODS bulk samples M1-M8 after SPS and homogenization annealing.

The XRD results of the bulk samples after SPS reveal a single-phase bcc structure (ferrite type, iron-based solid solution) in all investigated samples (Fig. 5). It is in agreement with most studies of FeCrAl alloys, e.g., FeCrAl ODS alloys with different Al content studied by S. Xu et al. [31] or FeCrAl ODS alloys with the addition of Ti investigated by C. Chen et al. [30]. It should be noted that the XRD patterns were acquired from 10° to 145° of 2Theta. However, between 10° and 35°, similarly, as for the powder samples, the background noise that originates mainly from the scattering of X-rays on air is more intense; therefore, the results for these angles are not shown after ensuring that no peaks are present between 10° and 35° of 2Theta. The lattice parameter of the bcc phases in the bulk samples is between 2.884 and 2.891 Å, which is closer to the bcc2 phase in mechanically alloyed powders and close to pure chromium. It shows a good homogenization of the bulk samples compared to the mechanically alloyed powders, which present two bcc phases with similar lattice parameters. The additions of alloying elements and their amounts seem not to have a significant impact on the lattice parameter. The crystallite size increases during consolidation from 10-30 nm in mechanically alloyed powder to above 100 nm in bulk samples. The peaks of oxides and carbides, which are undoubtedly present in the material, are not visible due to the low volume fraction and small size (mostly nanometric size) of these precipitates.

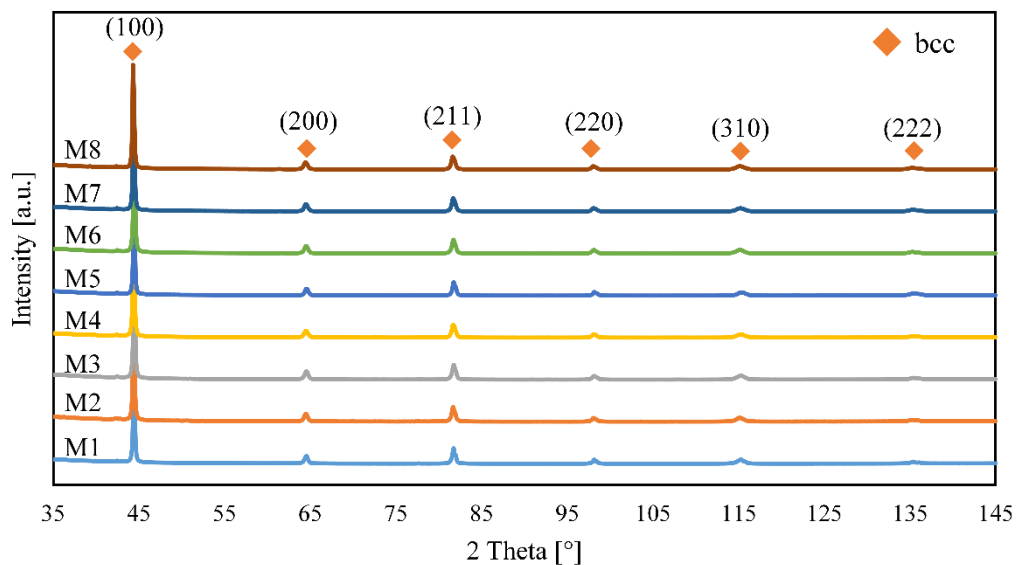


Fig. 5. XRD patterns of FeCrAl-Y₂O₃-Ti-V ODS bulk samples after SPS (samples M1-M8).

SEM microstructural observations (Fig. 6) confirm that the SPS consolidation at 1050°C of the mechanically alloyed powder led to high-density bulk samples. Nevertheless, some pores are present in bulk samples, which was confirmed by the observations realized with secondary electron mode (not shown here), which is typical for powder metallurgy materials prepared via sintering. The microstructure of FeCrAl-Y₂O₃-Ti-V ODS alloys is composed mainly of different size α -ferrite grains from sub-micrometric size to a few micrometer size (Figures 6a and 6b). Apart the matrix ferrite grains and large precipitates of size up to 1 μ m, homogeneously distributed nanoprecipitates are also visible. These precipitates also appear at the grain boundaries as chains and local aggregations. Microstructural observations of the samples after

annealing indicate that annealing at 1020°C does not significantly affect the structural and grain size changes in FeCrAl-ODS alloys. After the annealing process, a slightly higher amount of chain-like precipitates at grain boundaries and precipitates in the ferrite grains are visible, indicating precipitation effects during the annealing and air cooling.

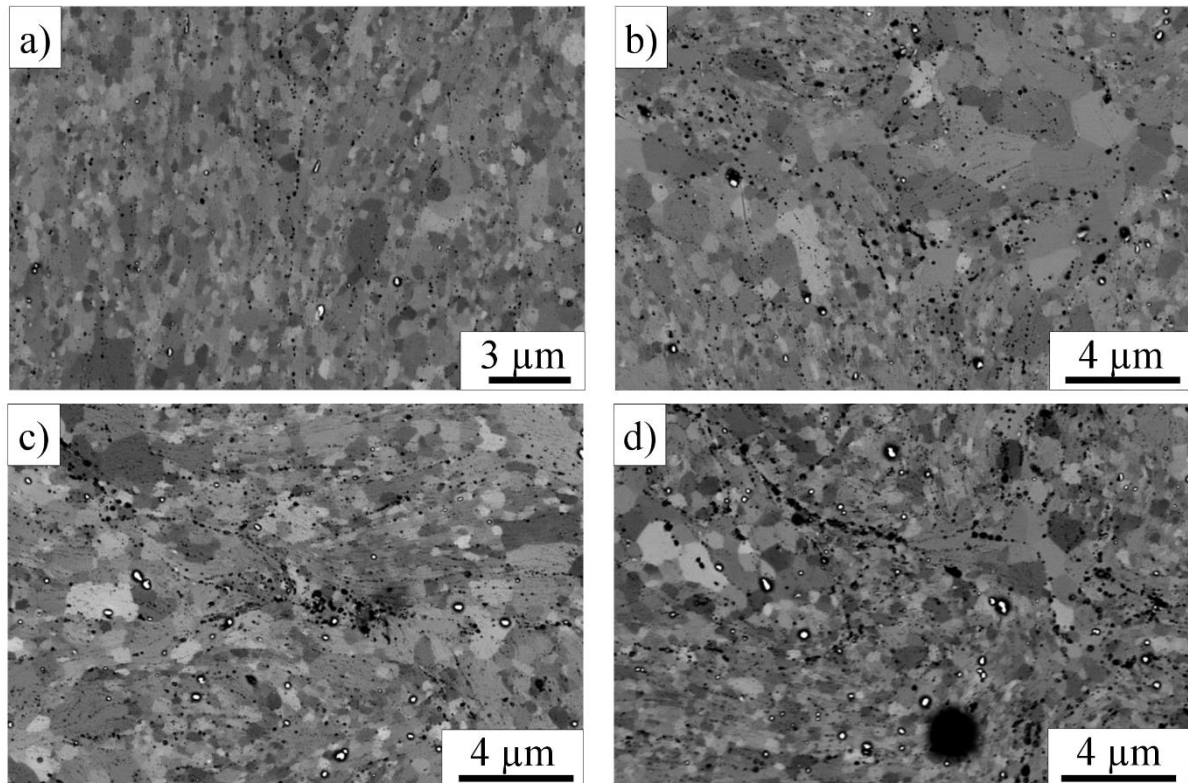


Fig. 6. SEM backscattered electron observations (performed using the working distance of 4 mm and accelerating voltage of 20 kV) of FeCrAl-Y₂O₃-Ti-V ODS bulk samples microstructure after SPS at 1050°C, the pressure of 40 MPa for 10 minutes and annealing at 1020°C for 30 min and air cooled; a) sample M4 after consolidation by SPS, b) sample M8 after consolidation by SPS, c) sample M4 after annealing, d) sample M8 after annealing.

EBSD observations, shown in Figure 7, confirm that, in addition to large micrometric α -ferrite grains, there are also areas in the FeCrAl ODS material where very fine submicron α -ferrite grains are accumulated. It is in agreement with the SEM observations (Figure 6). Inverse pole EBSD maps and grain size histograms indicate that SPS of MA powder-based ODS alloys at 1050°C resulted in the formation of randomly oriented grains and a bimodal grain size distribution, which is commonly known effect observed in SPS sintered ODS alloys observed by other researchers. E. Macía et al. [28] found bimodal grain size distribution (many grains of the size of approximately 300 nm and many grains of a few micrometers) in ODS samples containing oxide formers (Y, Ti, Al, Zr) prepared by mechanical alloying and SPS. H. Zhang et al. [23] obtained bimodal grain size distribution (many grains <500 nm and many grains 1–20 μ m) in Fe–14Cr–0.4Ti + 0.25Y₂O₃ alloy fabricated by mechanical alloying and consolidated by SPS. A. García-Junceda et al. [33], who studied Fe-14Cr-5Al-3W-0.4Ti-0.25Y₂O₃ with different additions of Zr prepared by mechanical alloying and spark plasma sintering, revealed a bimodal grain size distribution with grains of few hundreds of nanometers and grains with

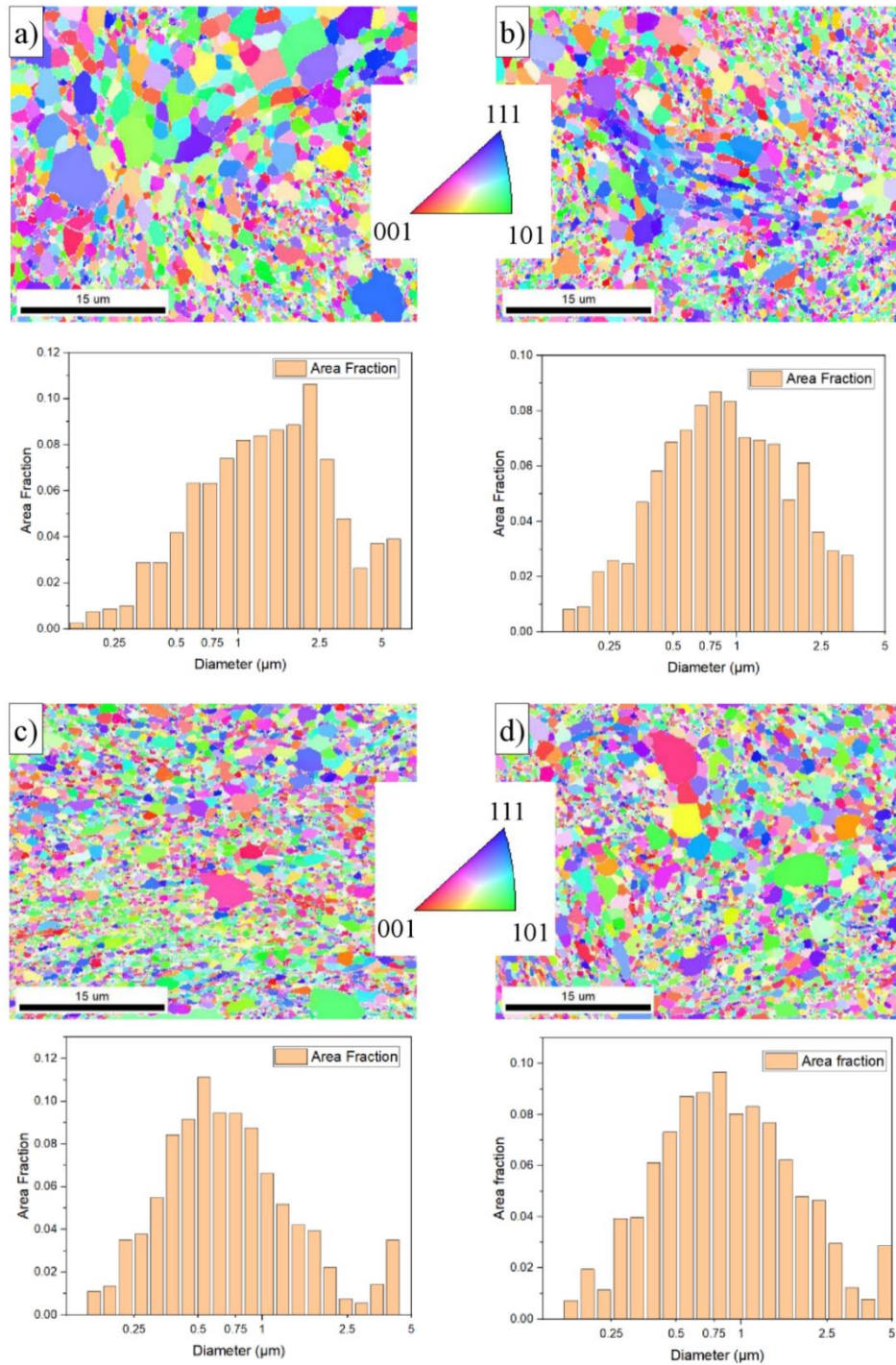


Fig. 7. EBSD results (acquired at the accelerating voltage of 15 kV using the working distance of approximately 10 mm with the sample tilted to 70°) of FeCrAl-ODS bulk samples after SPS and annealing at 1020°C for 30 min followed by air cooling: a) inverse pole figure map with the grain size distribution of sample M4 after SPS, b) inverse pole figure map with the grain size distribution of sample M8 after SPS, c) inverse pole figure map with the grain size distribution of sample M4 after annealing, d) inverse pole figure map with the grain size distribution of sample M8 after annealing.

few hundreds of micrometers. The bimodal grain size distribution in this study revealed by EBSD observations is essentially the result of uneven stress distribution in the grains during the mechanical alloying process and the fast non-equilibrium sintering process. In addition, this microstructure is also attributed to effects related to the formation of larger ferrite grains through grain growth in regions of lower nanoparticle density and inhomogeneity of their initial distribution, in which large grains capture adjacent smaller grains with higher energy. The EBSD analysis of the FeCrAl-Y₂O₃-Ti-V ODS alloys also made it possible to compare the grain size of the samples after SPS with the samples after the annealing process. Observations and analysis of average grain size histograms show that the annealing processes did not significantly change the grain size of FeCrAl ODS alloys. All grain sizes in the tested samples are in a similar range, as shown in Table 3.

Table 3. Average grain size estimated after SPS process and after annealing at 1020°C/30 min.

Sample	Average grain size after SPS [μm]	Average grain size after SPS and annealing [μm]
M1	0.53	0.75
M2	0.52	0.57
M3	0.51	0.54
M4	0.76	0.54
M5	0.62	0.61
M6	0.46	0.55
M7	0.65	0.64
M8	0.59	0.60

Interesting results of microstructure evaluation of FeCrAl-Y₂O₃-Ti-V ODS alloys were provided by SEM-EDS chemical composition mapping results for Fe, Cr, Ti, V, Y, and O, shown in Figure 8. The occurrence of micro- and nanoprecipitates indicated by SEM observations was well confirmed. As shown on the SEM-EDS maps, the dominant phase in the microstructure of the studied alloys is chromium-rich ferrite (α -Fe(Cr)). The maps also reveal nanoprecipitates and their arrangement at the grain boundaries. The SEM-EDS (Y-Ti-Al-O) maps in Figure 8 also show that zones enriched in Y, Ti, Al, and O are homogeneously dispersed in the FeCrAl ODS steel matrix. Qualitatively, Y, Ti, Al, and O enrichment areas coincided with Fe and Cr depletion areas. EDS maps show the presence of distinct (Y, Ti, O)-enriched clusters and (Y, Al, O)-enriched clusters. Although the vanadium is not visible in the EDS maps, its contribution will be confirmed in further studies by TEM-EDS. SEM-EDS maps also clearly revealed Al₂O₃ particles with significantly high Al and O content. It confirms that Al addition in the 2-6% range reacts with oxygen and tends to form aluminum oxides, which might significantly improve corrosion resistance in liquid metals and oxidation resistance of FeCrAl-based ODS alloys (according to the studies of A. Kimura et al. [39] in supercritical water and lead-bismuth eutectics, or according to the investigations of S. Takaya et al. [40] in lead-bismuth eutectics) and alumina forming austenitic steel [41]. The corrosion resistance of the investigated materials will be studied later. However, it is also known that Al addition could reduce the strength of ODS materials at high temperatures due to the formation of coarse-grained Y₄Al₂O₉ (YAM), Y₃Al₅O₁₂ (YAG), and Al₂O₃ particles. It also affects the thermal

aging embrittlement associated with ferritic alloys with high Cr content (>12%), as mentioned in the literature [21]. Ultimately, nanosized carbides and oxides in the matrix of ODS alloys may impede grain boundary migration, inhibiting grain growth of the matrix phase during creep and radiation operation. A. Meza et al. [3] studied 14Cr–5Al–3W with the addition of Zr and Ti and found exceptional creep resistance due to the presence of nanometric precipitates. Y. Li et al. [42] studied ODS alloys with 12% Cr and revealed that the fabrication conditions have a significant impact on the creep behavior; nevertheless, the presence of nanometric precipitates improves properties. M. Dash et al. [43] showed that the 18Cr alloy with nanometric oxide precipitates presents better creep resistance than 18Cr alloy without these precipitates and that the nanometric precipitates could limit grain growth at high temperatures. The authors wish to investigate behavior at high temperatures in later experiments related to heat treatment, aging processes, high-temperature corrosion, and creep tests of studied ODS alloys. Moreover, the irradiation experiments will be planned to evaluate the behavior of the ODS alloys.

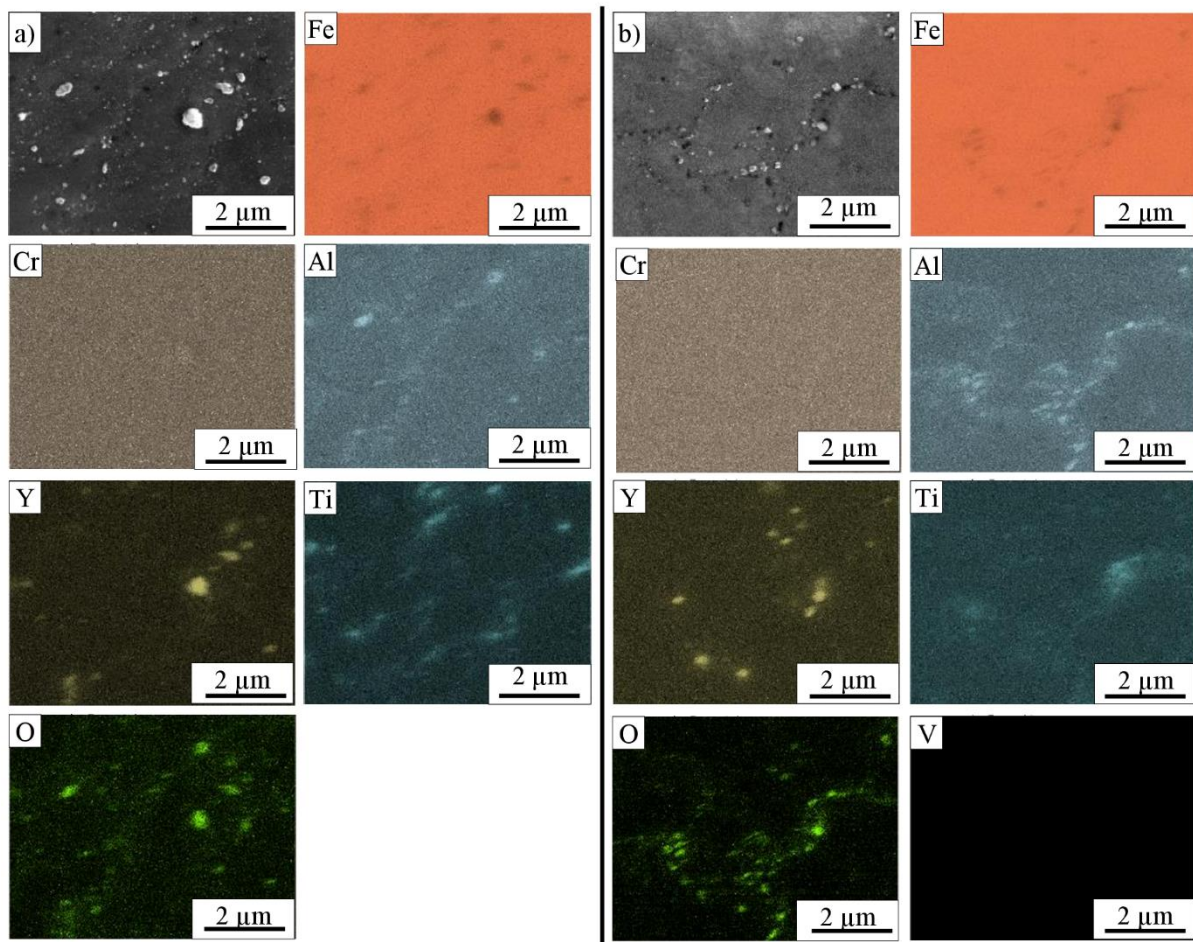


Fig. 8. SEM-EDS maps acquired using the accelerating voltage of 15 kV and the working distance of 4 mm of FeCrAl-Y₂O₃-Ti-V ODS alloys after SPS revealing the presence of different types of oxides: a) M3 sample and b) M6 sample.

The TEM and STEM results (Fig. 9) show sub-micrometer fine grains and some larger micrometric grains of the bcc matrix phase. It agrees with SEM and EBSD analyses of the bulk samples after consolidation by SPS and homogenization annealing at 1020°C for 30 minutes.

A considerable variation in grain size is typical for the powder metallurgy-prepared samples, especially those prepared with SPS by H. Zhang et al. [23] (small grains below 500 nm and large grains between 1 and 20 μm), E. Macía et al. [28] (grains from a few hundred nanometers to a few dozen micrometers), and X. Boulnat et al. [44] (grains from 50 nm to approximately 1 μm for the SPS at 850°C, and grains from a few hundred nanometers to 20-25 μm for the SPS at 1050°C and 1150°C), and even the homogenization annealing did not result in significant changes in the grain size. The high magnification TEM/STEM observations reveal a high volume fraction of nanometric precipitates (up to 100 nm) in all investigated samples, i.e., up to 2.57% in the M8 sample after SPS and up to 2.64% in the M8 sample after homogenization annealing. The nanometric precipitates are homogeneously distributed in the matrix bcc phase. A slightly higher volume fraction of precipitates after annealing could be the effect of precipitation during heat treatment. Most nanometric precipitates are located inside the grains of the matrix bcc phase (intra-granular precipitates). These high-density precipitates can improve mechanical strength without increasing brittleness and can increase the material's thermal stability. The increase in strength and thermal stability due to nanometric precipitates was revealed by studies of the Fe-18Cr-2W-0.25Ti-0.1C-0.35Y₂O₃ ODS ferritic steels by M. Dash et al. [43]. X. Boulnat et al. [44] revealed that nanometric precipitates pin grain boundaries, preventing grain growth and, therefore, improving the mechanical properties and thermal stability of the alloy. Moreover, nano-precipitates can act as sinks for irradiation-induced defects during the operation of nuclear reactors. Z. Ding et al. [20], who studied ODS alloys under irradiation, showed that the alloy with a higher density of nanometric oxides presents smaller hardening under irradiation. It confirms that these precipitates could act as sinks for defects. C. Heintze et al. [45], who studied Eurofer97 without oxide precipitates and Eurofer ODS under Fe and He irradiation, revealed that the increase of hardness after irradiation in ODS material is less pronounced than in nanometric dispersion-free material. Thus, it shows that nanometric precipitates could improve irradiation resistance. Moreover, oxide precipitates, due to the high interface surface area between them and ferrite, could reduce void swelling phenomena by trapping and managing helium atoms [46]. Therefore, nanometric particles are beneficial not only in improving mechanical properties but also in a significant increase in the irradiation resistance of FeCrAl-Y₂O₃-Ti-V ODS alloys applied in nuclear conditions. However, the precipitates at the grain boundaries (inter-granular precipitates) are also present in the studied samples. These inter-granular particles seem to be larger than the intra-granular precipitates. Some of their sizes are more than 100 nm. In Fig. 9b, a large inter-granular particle is identified as Y₂O₃. Larger precipitates are not desired in engineering materials due to their role in increasing brittleness, although they are difficult to avoid in powder metallurgy processing.

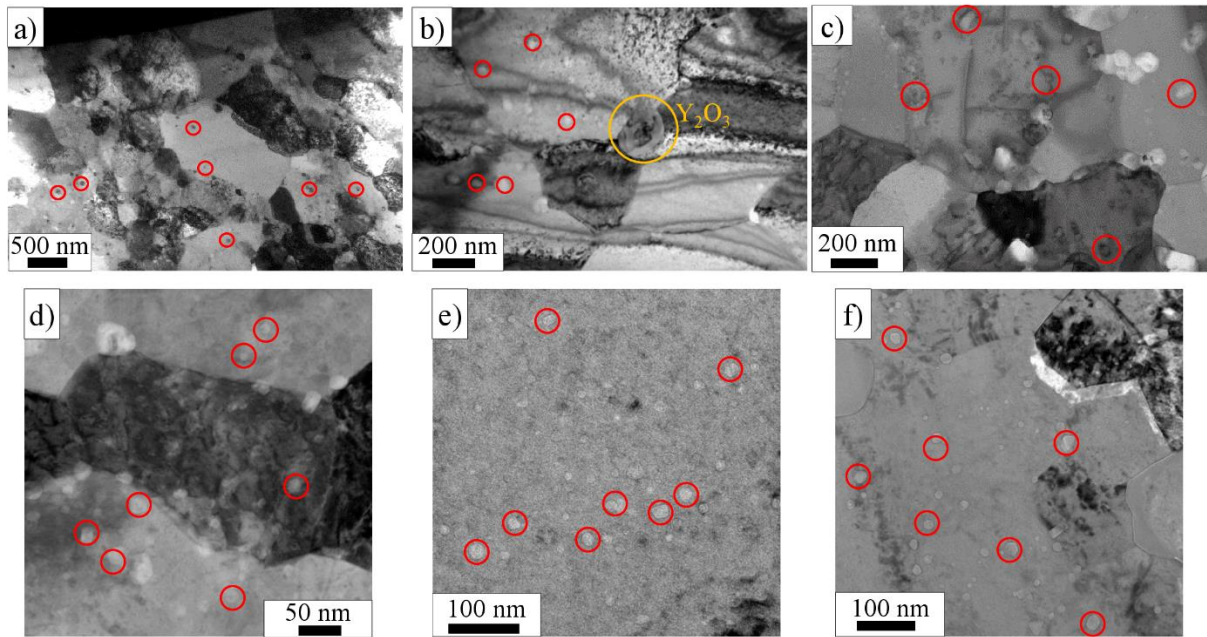


Fig. 9. TEM/STEM images of FeCrAl-Y₂O₃-Ti-V ODS microstructure showing nanometric precipitates (some of them highlighted in red): a) TEM bright image of the M4 sample after SPS, b) TEM bright image of the M8 sample after SPS, c) STEM image of the M4 sample after SPS, d) STEM image of the M8 sample after SPS, e) TEM bright field image of M4 sample after annealing, and f) under-focused TEM bright field image of the M8 sample after annealing.

The results of measurements of nanometric precipitate size (<100 nm) based on multiple TEM and STEM images reveal that most particles are in size between 20 and 50 nm. The histograms of precipitate size in the M8 sample after SPS and after annealing are shown in Fig. 10. It seems that the variation of the chemical composition in investigated samples does not significantly impact the size distribution of oxide and carbide precipitates. The size between 20 and 50 nm is expected to be optimal to increase irradiation resistance and improve mechanical resistance without causing significant brittleness. It should be noted that no increase in the size of precipitates was found after annealing.

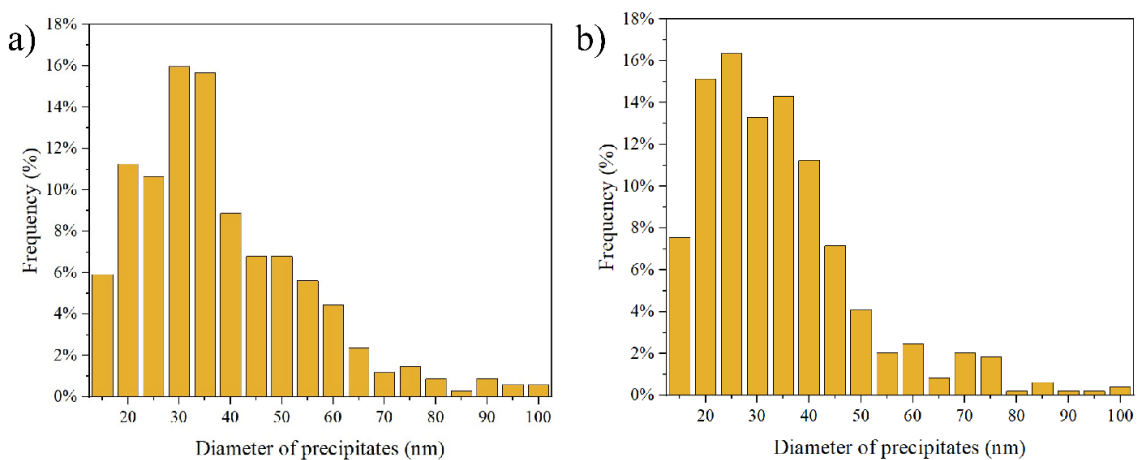


Fig. 10. Size distribution of nanometric precipitates (<100 nm) in the M8 sample: a) after SPS, b) after annealing at 1020°C for 30 minutes.

The conducted STEM-EDS analyses (Fig. 11) enable a better characterization of the chemical composition of nanometric precipitates, which is impossible using SEM-EDS due to the very limited resolution of this technique. Determining the composition of nanometric precipitates is crucial in the investigation of ODS materials and has been studied in many other papers. In most ODS alloys, different types of nanometric particles are present, e.g., Y-Al-O oxides in the studies by S. Xu et al. [31], Y_2O_3 and MnO in the investigations by A. Mori et al. [38], Y-Ti-O (mainly $Y_2Ti_2O_7$) in the paper by H. Zhang et al. [23], and Y-Ti-O, Ti-O, Ti-V-O, Cr-V-O in the studies by Z. Oksiuta et al. [18]. The selected area electron diffraction (SAED) is also very limited in characterizing the crystallographic structure of precipitates due to their small size. In this study, the SAED was conducted only on the largest particles (size of a few hundred micrometers). The SAED patterns (not shown here) reveal that the largest precipitates are Y_2O_3 ; however, they are rarely distributed, and only two or three such particles were found in each FIB lamella.

The STEM-EDS results show that the most precipitates are significantly enriched in Al. Some regions enriched in Al coincide with zones enriched in Y, which can suggest the formation of complex Al-Y-O oxides. These types of oxides are commonly found in ODS materials. J. Wang et al. [19], who studied 9Cr-3Al-ODS alloys with the addition of Zr prepared by mechanical alloying and hot isostatic pressing, found the presence of Al-Y-O, i.e., $Y_4Al_2O_9$ and $Y_3Al_5O_{12}$ with the average size between 9 and 17 nm. N. García-Rodríguez et al. [27], who studied different compositions of FeCrAl ODS alloys with the additions of Y_2O_3 , Ti, and W, found the formation of several nanometric Y-Al-O precipitates in mechanically alloyed and SPSed samples. These precipitates were identified as $Y_2Al_4O_9$, $YAlO_3$, and $Y_2Al_5O_{12}$. S. Xu et al. [31], who studied FeCrAl ODS alloys prepared by mechanical alloying and consolidated by hot isostatic pressing, found two types of $YAlO_3$, one with a hexagonal structure and the other with an orthorhombic structure. Both oxides present the nanometric size between a few nanometers and 40 nm. M. Gong et al. [47], who studied 14Cr-ODS alloys with the addition of Al, Ti, W, and Y_2O_3 , found Y-Al-O-rich precipitates in size between 10 and 70 nm. The analyses also reveal regions enriched in Ti-Y-O, evident in the M4 sample (Fig. 11a). In other studies of ODS alloys, these oxides are also commonly found, e.g., fine Y-Ti-O with less than 30 nm in 14Cr-Ti-ODS steel in the article by M. Gong et al. [47]; Y-Ti-O precipitates in the study of their evolution by S. Oh et al. [48], $Y_2Ti_2O_7$ nanoparticles in the investigations by K. Hong et al. [49], very small clusters of 3-5 nm of Y-Ti-O in the studies by D. Larson et al. [50]. According to investigations in the literature by TEM and atom probe tomography (APT), which is a more powerful tool in terms of chemical composition analysis, the small Ti-Y-O regions could be $Y_2Ti_2O_7$ pyrochlore phase showing face-centered cubic phase, and the bigger Ti-Y-O regions could be Y_2TiO_5 [51]. Larger precipitates containing Ti without Y can also be found (Fig. 11a). These larger precipitates seem to be significantly enriched in C, suggesting the formation of titanium-rich carbides. Ti-rich carbide precipitates are rarely present in other papers about ODS alloys, e.g., Ti-rich MC-type carbides in additively manufactured ODS alloys found by J. Lopez et al. [52] or Ti/Nb-rich carbides at grain boundaries of additively manufactured alloy by T. Smith et al. [53]. In the samples with the addition of vanadium, vanadium-rich precipitates can also be found (Fig. 11b). The vanadium-rich areas coincide with the region rich in titanium and

zones rich either in oxygen or carbon. Therefore, it suggests the formation of vanadium-titanium-rich oxides and carbides. It should be noted that no precipitates enriched in Cr are found in the investigated samples. However, in many papers exploring ODS materials, Cr-rich precipitates are spotted, e.g., M. Auger et al. [54] found Cr_2O_3 precipitates at the grain boundaries in ODS alloy produced by powder metallurgy, in another work by M. Auger et al. [55] found Cr-rich precipitates (mostly Cr_2O_3) in size between 60 and 300 nm, L. Kurpaska et al. [56] observed Cr-O-V and Cr-C-V nanometric precipitates.

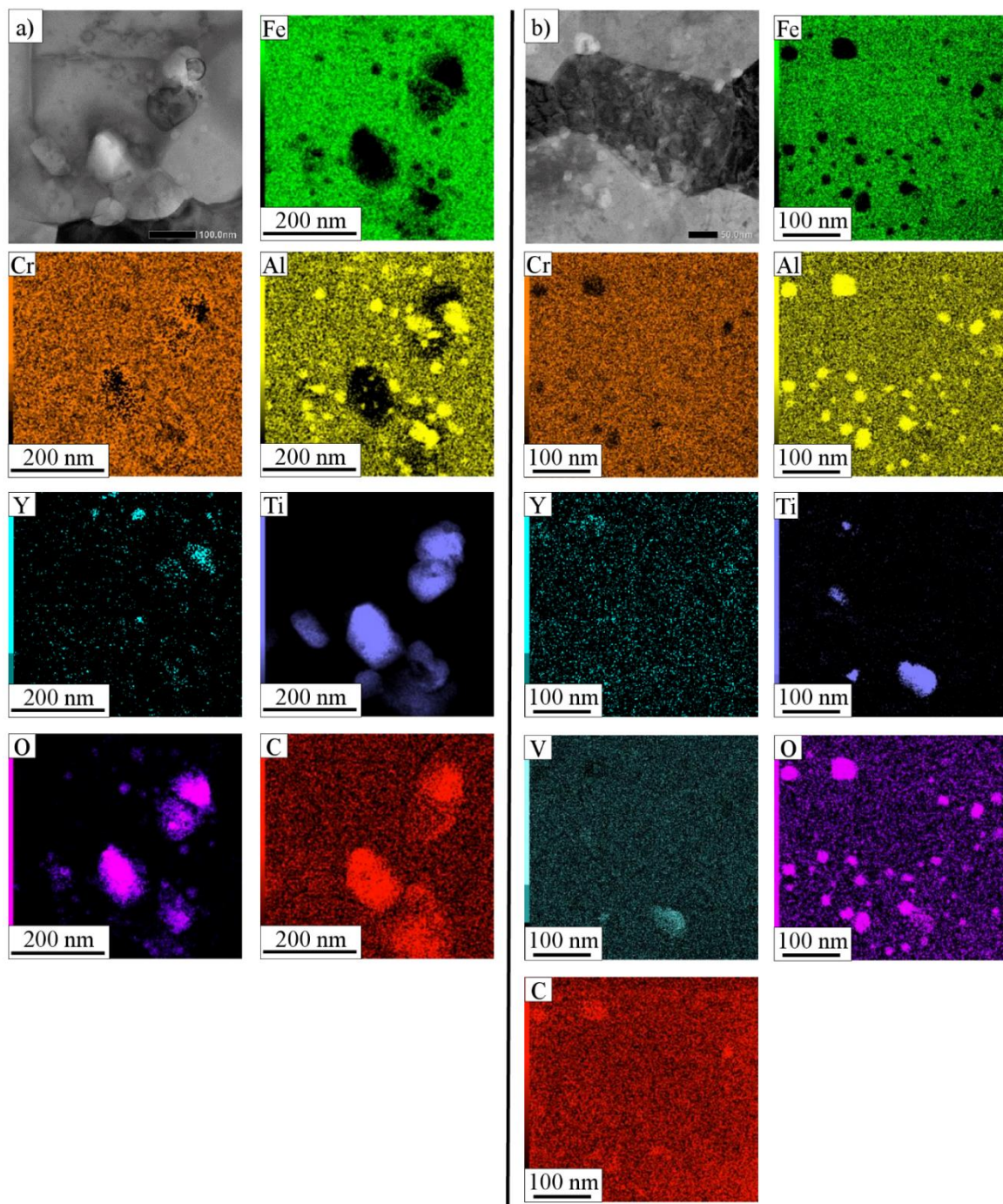


Fig. 11. STEM-EDS analyses of FeCrAl- Y_2O_3 -Ti-V ODS revealing different types of nanometric precipitates: a) M4 sample after SPS, b) M8 samples after SPS.

3.3. Hardness measurements and nanoindentation results

The Vickers microhardness (HV0.5) results (Fig. 12) reveal the microhardness between 267 and 376 HV0.5. The content of chromium and minor alloying elements (Ti and V) have no visible effect on the microhardness of samples in an as-sintered state (SPS). The composition differences among samples seem too small, i.e., 9-12% of Cr, 0.5-1% of Ti, and 0-0.5% of V, to establish a firm relation between the composition and mechanical properties in an as-sintered state. However, the influence of alloying elements is better visible after homogenization annealing at 1020°C for 30 min. The hardness of the samples without the addition of vanadium (except for the M4 sample) decreases slightly after annealing. It is probably the effect of the slight increase of the grain size (confirmed by EBSD analyses), although the relative density increases slightly after annealing (Fig. 4). The hardness of samples containing 0.5% vanadium (M5-M8) increases after annealing. It could be the effect of the formation of additional vanadium-rich precipitates during heat treatment. TEM analyses reveal a slightly higher volume fraction of precipitates after annealing. Nevertheless, it should be noted that the hardness increase is minimal. Even though the impact of the differences in chemical composition is not very visible at this stage of investigations, the effects are expected to be better visible after different annealing campaigns, which are planned for future experiments with these produced ODS materials. The chromium content (either 9 or 12%) could have a critical impact on “475°C embrittlement” related to phases separation to α and α' , Fe-rich and Cr-rich [57]. The addition of alloying elements (Ti and V) could be crucial in forming precipitates during long-time annealing (e.g., ≥ 1000 h), which can have a substantial impact on the thermal stability of the material or creep resistance. Nevertheless, the hardness of the investigated samples is comparable to many other ODS alloys prepared by powder metallurgy, e.g., FeCrAl ODS alloy with 7% Al prepared by mechanical alloying and hot extrusion reveals the hardness of 325 HV₂ [58], FeCrAl ODS alloys fabricated by mechanical alloying and hot isostatic pressing show the hardness of 305 HV₁ [30], or 9Cr-1Mo ferritic-martensitic ODS steel prepared by mechanical alloying, hot isostatic pressing, and hot rolling reveals hardness of about 320 HV [59].

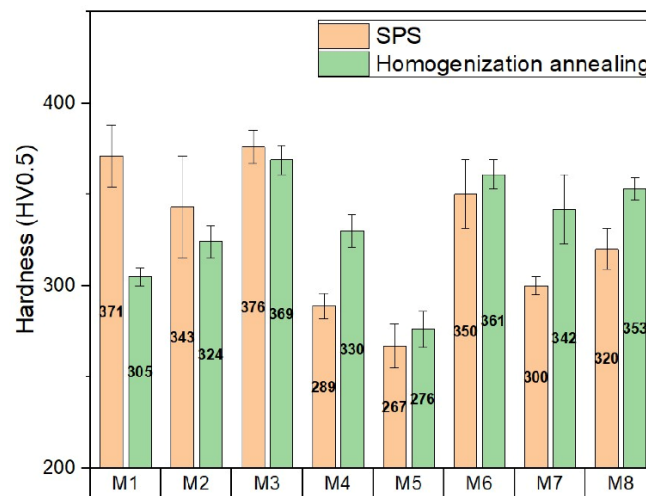


Fig. 12. Vickers microhardness results of the FeCrAl-Y₂O₃-Ti-V ODS samples after SPS and annealing at 1020°C/30 min.

The nanoindentation experiments allow the determination of the hardness and reduced Young's modulus of the investigated ODS materials (Fig. 13). The results show that the hardness of SPS samples decreases with increasing load (a deeper contact depth). It is a commonly observed relation known as the indentation size effect (ISE) [60]. However, the hardness of the annealed samples is almost stable, and the ISE is not visible. The hardness of the M4 sample (Fig. 13a) after annealing (4.01 ± 0.22 GPa) is slightly higher than the hardness after SPS (3.78 ± 0.34 GPa) for the highest contact depth (290-310 nm). It is in agreement with the Vickers microhardness results (Fig. 12), revealing an increase in the hardness of this sample after annealing. However, the hardness results of the M8 sample (Fig. 13b) for the highest contact depth (270-280 nm) show a slight decrease of hardness after annealing, i.e., 4.83 ± 0.43 GPa for the SPS sample vs. 4.33 ± 0.44 GPa. It is in slight opposition to the Vickers microhardness results, which suggest an increase in hardness.

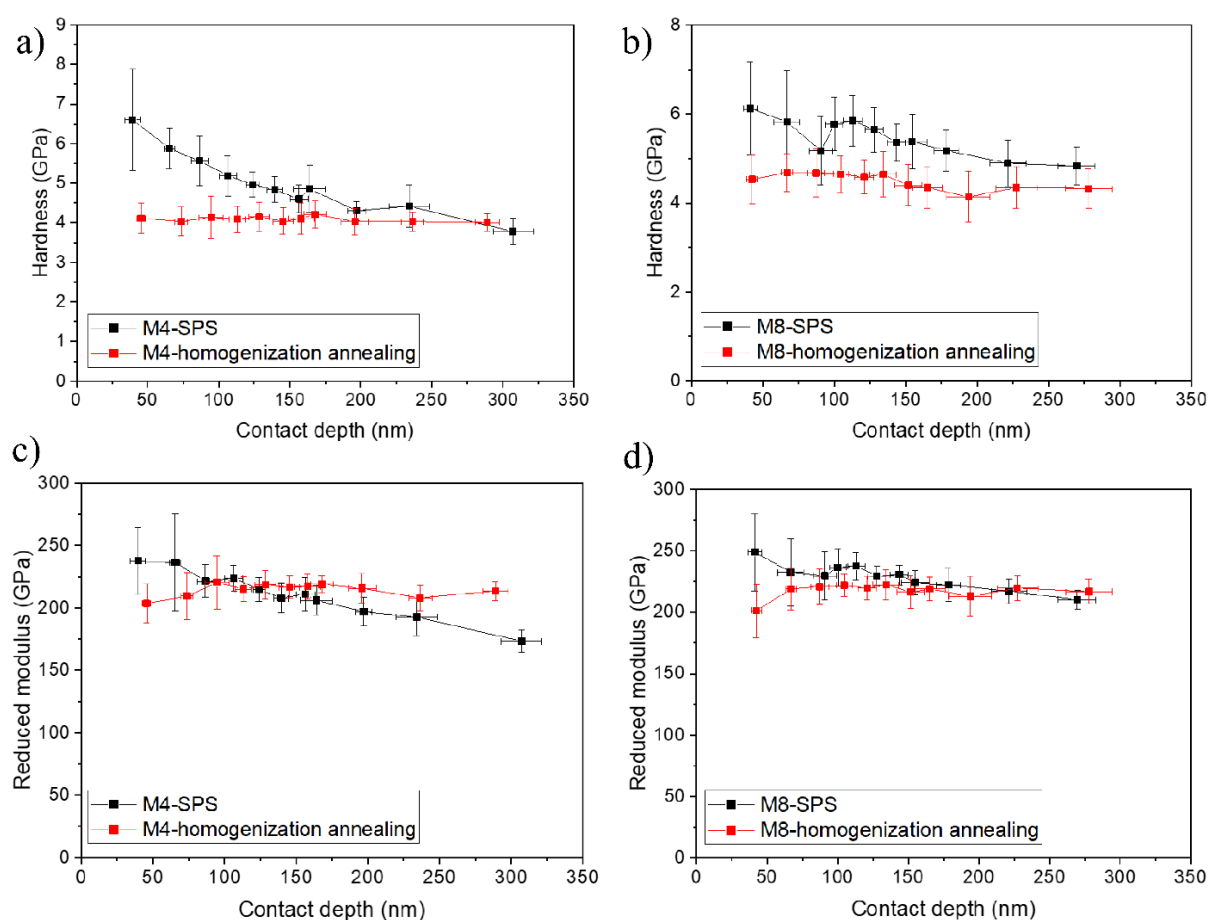


Fig. 13. Nanoindentation results of the FeCrAl-Y₂O₃-Ti-V ODS alloys after SPS and after homogenization annealing at 1020°C for 30 minutes: a) hardness of the M4 sample, b) hardness of the M8 sample, c) reduced Young's modulus of the M4 sample, d) reduced Young's modulus of the M8 sample.

The reduced Young's modulus results show a similar trend (as a function of contact depth) as hardness (Fig. 13c, d). For the samples after SPS, the values of reduced Young's modulus are rather decreasing with increasing contact depth (increasing load). In contrast, the values are

relatively stable for the samples after homogenization annealing. Moreover, the reduced Young's modulus is slightly higher (for the highest contact depth) in the samples after homogenization, i.e., for the M4 samples: 173 ± 9 GPa after SPS vs. 214 ± 7 GPa after annealing and for the M8 samples: 210 ± 7 GPa after SPS vs. 217 ± 10 GPa. Therefore, it should be noted that the homogenization annealing does not have an essential impact on hardness or reduced Young's modulus values except for the suppression of indentation size effect, which means the values of hardness and reduced Young's modulus are relatively stable as a function of the contact depth.

4. Conclusions

The investigation showed the successful preparation of FeCrAl-Y₂O₃ ODS alloys with Ti and V additions by powder metallurgy (mechanical alloying and SPS) and controlled heat treatment. The mechanically alloyed powders consist of two bcc solid solutions with similar lattice parameters, confirming the correctly selected mechanical alloying parameters. Powder analysis results showed a significant decrease in crystallite size from 74 nm (pure Fe powder) to about 25 nm during mechanical alloying. The obtained powders were homogeneous, as the SEM-EDS micro areas chemical analysis confirmed. The consolidated samples and the annealed samples show good densification (density of about 96%) and a fine microstructure of α -ferrite with the majority of grains below 1 μ m. In addition, the analysis revealed a bimodal distribution of α -ferrite grains after SPS consolidation. In turn, the heat treatment did not significantly affect the bimodal microstructure and grain size. The microstructural analysis showed the presence of nanometric precipitates and their homogeneous distribution in the matrix, which should substantially impact the creep strength and radiation resistance during operation in nuclear conditions. In both groups of materials (after SPS and after subsequent annealing), many nano- (20-50 nm) and micro- (up to 1 μ m) oxide and carbide precipitates are formed, both in the matrix grains and at the grain boundaries. There is no growth of precipitates during annealing. Performed hardness tests show that the addition of V has a positive effect on the increase in the hardness after annealing (on average by about 24 HV0.5).

Statements and Declarations

Acknowledgements

The research leading to these results was carried out in the frame of the SafeG project and is partly funded by the European Commission Horizon 2020 Framework Programme under grant agreement No. 945041.

The authors: Jaroslaw J. Jasinski, Lukasz Kurpaska, Magdalena Wilczopolska, Katarzyna Mulewska, Maciej Zielinski, and Jacek Jagielski acknowledge the support from the European Union Horizon 2020 research and innovation program under NOMATEN Teaming grant agreement no. 857470 and from the European Regional Development Fund via the Foundation for Polish Science International Research Agenda Plus program grant no. MAB PLUS/2018/8 which partially covered their salaries during preparation of this article.

Dr. Anna Kosińska is acknowledged for her help in performing and analyzing electron microscopy images.

Conflict of interest

The authors declare that they have no known competing financial interests or personal relationships that could have appeared to influence the work reported in this paper.

Ethical approval

This article does not contain any studies with human participants or animals performed by any of the authors.

References

- [1] Abram T, Ion S. Generation-IV nuclear power: A review of the state of the science. *Energy Policy* 2008;36:4323–30. doi:10.1016/J.ENPOL.2008.09.059.
- [2] Yvon P, Carré F. Structural materials challenges for advanced reactor systems. *J Nucl Mater* 2009;385:217–22. doi:10.1016/J.JNUCMAT.2008.11.026.
- [3] Meza A, Macía E, Chekonin P, Altstadt E, Rabanal ME, Torralba JM, Campos M. The effect of composition and microstructure on the creep behaviour of 14 Cr ODS steels consolidated by SPS. *Mater Sci Eng A* 2022;849:143441. doi:10.1016/J.MSEA.2022.143441.
- [4] Sakamoto K, Miura Y, Ukai S, Oono NH, Kimura A, Yamaji A, Kusagaya K, Takano S, Kondo T, Ikegawa T, Ioka I, Yamashita S. Development of accident tolerant FeCrAl-ODS fuel cladding for BWRs in Japan. *J Nucl Mater* 2021;557:153276. doi:10.1016/J.JNUCMAT.2021.153276.
- [5] Rahman MM, Dongxu J, Jahan N, Salvatores M, Zhao J. Design concepts of supercritical water-cooled reactor (SCWR) and nuclear marine vessel: A review. *Prog Nucl Energy* 2020;124:103320. doi:10.1016/J.PNUCENE.2020.103320.
- [6] Isselin J, Kasada R, Kimura A. Corrosion behaviour of 16%Cr–4%Al and 16%Cr ODS ferritic steels under different metallurgical conditions in a supercritical water environment. *Corros Sci* 2010;52:3266–70. doi:10.1016/J.CORSCI.2010.05.043.
- [7] Hino T, Miwa J, Mitsuyasu T, Ishii Y, Ohtsuka M, Moriya K, Shirvan K, Seker V, Hall A, Downar T, Gorman PM, Fratoni M, Greenspan E. Core Design and Analysis of Axially Heterogeneous Boiling Water Reactor for Burning Transuranium Elements. *Nucl Sci Eng* 2017;187:213–39. doi:10.1080/00295639.2017.1312941.
- [8] Maréchal L, Lesage B, Huntz AM, Molins R. Oxidation behavior of ODS Fe-Cr-Al alloys: Aluminum depletion and lifetime. *Oxid Met* 2003;60:1–28. doi:10.1023/A:1024604428747/METRICS.
- [9] Terrani KA. Accident tolerant fuel cladding development: Promise, status, and challenges. *J Nucl Mater* 2018;501:13–30. doi:10.1016/J.JNUCMAT.2017.12.043.
- [10] Kane KA, Lee SK, Bell SB, Brown NR, Pint BA. Burst behavior of nuclear grade FeCrAl and Zircaloy-2 fuel cladding under simulated cyclic dryout conditions. *J Nucl Mater* 2020;539:152256. doi:10.1016/J.JNUCMAT.2020.152256.
- [11] Kobayashi S, Takasugi T. Mapping of 475 °C embrittlement in ferritic Fe–Cr–Al alloys. *Scr Mater* 2010;63:1104–7. doi:10.1016/J.SCRIPTAMAT.2010.08.015.
- [12] Han W, Yabuuchi K, Kimura A, Ukai S, Oono N, Kaito T, Torimaru T, Hayashi S.

- Effect of Cr/Al contents on the 475°C age-hardening in oxide dispersion strengthened ferritic steels. *Nucl Mater Energy* 2016;9:610–5. doi:10.1016/J.NME.2016.05.015.
- [13] Li W, Lu S, Hu QM, Mao H, Johansson B, Vitos L. The effect of Al on the 475 °C embrittlement of Fe–Cr alloys. *Comput Mater Sci* 2013;74:101–6. doi:10.1016/J.COMMATSCI.2013.03.021.
- [14] Wang X, Lu Z, Li Z, Shi Y, Xu H. Effect of Zr content on microstructure and hardness of ODS-FeCrAl alloys. *Mater Charact* 2022;192:112221. doi:10.1016/J.MATCHAR.2022.112221.
- [15] Yang TX, Li ZX, Zhou CJ, Xu YC, Dou P. Effects of Zr and/or Ti addition on the morphology, crystal and metal/oxide interface structures of nanoparticles in FeCrAl-ODS steels. *J Nucl Mater* 2023;585:154613. doi:10.1016/J.JNUCMAT.2023.154613.
- [16] Massey CP, Edmondson PD, Unocic KA, Yang Y, Dryepontd SN, Kini A, Gault B, Terrani KA, Zinkle SJ. The effect of Zr on precipitation in oxide dispersion strengthened FeCrAl alloys. *J Nucl Mater* 2020;533:152105. doi:10.1016/J.JNUCMAT.2020.152105.
- [17] Jasinski JJ, Stasiak T, Chmurzynski W, Kurpaska L, Chmielewski M, Frelek-Kozak M, Wilczopolska M, Mulewska K, Zielinski M, Kowal M, Diduszko R, Chrominski W, Jagielski J. Microstructure and phase investigation of FeCrAl-Y2O3 ODS steels with different Ti and V contents. *J Nucl Mater* 2023;586:154700. doi:10.1016/J.JNUCMAT.2023.154700.
- [18] Oksiuta Z, Lewandowska M, Kurzydowski KJ, Baluc N. Effect of vanadium addition on the microstructure and mechanical properties of the ODS ferritic steels. *J Nucl Mater* 2013;442:S84–8. doi:10.1016/J.JNUCMAT.2012.10.022.
- [19] Wang J, Long D, Yu L, Liu Y, Li H, Wang Z. Influence of Al addition on the microstructure and mechanical properties of Zr-containing 9Cr-ODS steel. *J Mater Res Technol* 2021;13:1698–708. doi:10.1016/J.JMRT.2021.05.112.
- [20] Ding ZN, Zhang CH, Yang YT, Song Y, Kimura A, Jang J. Hardening of ODS ferritic steels under irradiation with high-energy heavy ions. *J Nucl Mater* 2017;493:53–61. doi:10.1016/J.JNUCMAT.2017.05.040.
- [21] Capdevila C, Aranda MM, Rementeria R, Domínguez-Reyes R, Urones-Garrote E, Miller MK. Influence of nanovoids on α - α' phase separation in FeCrAl oxide dispersion strengthened alloy. *Scr Mater* 2016;110:53–6. doi:10.1016/J.SCRIPTAMAT.2015.07.044.
- [22] Frelek-Kozak M, Kurpaska L, Wyszowska E, Jagielski J, Pawlak W, Jozwik I, Chmielewski M, Perkowski K, Lewandowska M. Influence of consolidation process on functional properties of steels. *Surf Coatings Technol* 2018;355:234–9. doi:10.1016/J.SURFCOAT.2018.02.049.
- [23] Zhang H, Huang Y, Ning H, Williams CA, London AJ, Dawson K, Hong Z, Gorley MJ, Grovenor CRM, Tatlock GJ, Roberts SG, Reece MJ, Yan H, Grant PS. Processing and microstructure characterisation of oxide dispersion strengthened Fe–14Cr–0.4Ti–0.25Y2O3 ferritic steels fabricated by spark plasma sintering. *J Nucl Mater* 2015;464:61–8. doi:10.1016/J.JNUCMAT.2015.04.029.
- [24] Frelek-Kozak M, Kurpaska L, Mulewska K, Zieliński M, Diduszko R, Kosińska A, Kalita D, Chromiński W, Turek M, Kaszyca K, Zaborowska A, Jagielski J. Mechanical

- behavior of ion-irradiated ODS RAF steels strengthened with different types of refractory oxides. *Appl Surf Sci* 2023;610:155465. doi:10.1016/J.APSUSC.2022.155465.
- [25] Das A, Chekhonin P, Altstadt E, McClintock D, Bergner F, Heintze C, Lindau R. Microstructure and fracture toughness characterization of three 9Cr ODS EUROFER steels with different thermo-mechanical treatments. *J Nucl Mater* 2020;542:152464. doi:10.1016/J.JNUCMAT.2020.152464.
- [26] Ohtsuka S, Kaito T, Inoue M, Asayama T, Kim SW, Ukai S, Narita T, Sakasegawa H. Effects of aluminum on high-temperature strength of 9Cr–ODS steel. *J Nucl Mater* 2009;386–388:479–82. doi:10.1016/J.JNUCMAT.2008.12.147.
- [27] García-Rodríguez N, Campos M, Torralba JM, Berger MH, Bienvenu Y. Capability of mechanical alloying and SPS technique to develop nanostructured high Cr, Al alloyed ODS steels. *Mater Sci Technol* 2014;30:1676–84. doi:10.1179/1743284714Y.0000000595.
- [28] Macía E, García-Junceda A, Serrano M, Hernández-Mayoral M, Diaz LA, Campos M. Effect of the heating rate on the microstructure of a ferritic ODS steel with four oxide formers (Y-Ti-Al-Zr) consolidated by spark plasma sintering (SPS). *J Nucl Mater* 2019;518:190–201. doi:10.1016/J.JNUCMAT.2019.02.043.
- [29] Suryanarayana C. Mechanical alloying and milling. *Prog Mater Sci* 2001;46:1–184. doi:10.1016/S0079-6425(99)00010-9.
- [30] Chen CL, Dong YM. Effect of mechanical alloying and consolidation process on microstructure and hardness of nanostructured Fe–Cr–Al ODS alloys. *Mater Sci Eng A* 2011;528:8374–80. doi:10.1016/J.MSEA.2011.08.041.
- [31] Xu S, Zhou Z, Jia H, Yao Z. Microstructure Characterization and Mechanical Properties of Al Alloyed 9Cr ODS Steels with Different Al Contents. *Steel Res Int* 2019;90:1800594. doi:10.1002/SRIN.201800594.
- [32] Wyszowska E, Kurpaska L, Frelek-Kozak M, Jozwik I, Perkowski K, Jagielski J. Investigation of the mechanical properties of ODS steels at high temperatures using nanoindentation technique. *Nucl Instruments Methods Phys Res Sect B Beam Interact with Mater Atoms* 2019;444:107–11. doi:10.1016/J.NIMB.2019.02.021.
- [33] García-Junceda A, Macía E, Garbiec D, Serrano M, Torralba JM, Campos M. Effect of Small Variations in Zr Content on the Microstructure and Properties of Ferritic ODS Steels Consolidated by SPS. *Metals (Basel)* 2020;10:348. doi:10.3390/MET10030348.
- [34] Gates-Rector S, Blanton T. The Powder Diffraction File: a quality materials characterization database. *Powder Diffr* 2019;34:352–60. doi:10.1017/S0885715619000812.
- [35] Oliver WC, Pharr GM. An improved technique for determining hardness and elastic modulus using load and displacement sensing indentation experiments. *J Mater Res* 1992;7:1564–83. doi:10.1557/JMR.1992.1564.
- [36] Munir ZA, Anselmi-Tamburini U, Ohyanagi M. The effect of electric field and pressure on the synthesis and consolidation of materials: A review of the spark plasma sintering method. *J Mater Sci* 2006;41:763–77. doi:10.1007/S10853-006-6555-2.
- [37] Sun QX, Zhang T, Wang XP, Fang QF, Hao T, Liu CS. Microstructure and mechanical

- properties of oxide dispersion strengthened ferritic steel prepared by a novel route. *J Nucl Mater* 2012;424:279–84. doi:10.1016/J.JNUCMAT.2011.12.020.
- [38] Mori A, Mamiya H, Ohnuma M, Ilavsky J, Ohishi K, Woźniak J, Olszyna A, Watanabe N, Suzuki J, Kitazawa H, Lewandowska M. Manufacturing and characterization of Ni-free N-containing ODS austenitic alloy. *J Nucl Mater* 2018;501:72–81. doi:10.1016/J.JNUCMAT.2018.01.025.
- [39] Kimura A, Kasada R, Iwata N, Kishimoto H, Zhang CH, Isselin J, Dou P, Lee JH, Muthukumar N, Okuda T, Inoue M, Ukai S, Ohnuki S, Fujisawa T, Abe TF. Development of Al added high-Cr ODS steels for fuel cladding of next generation nuclear systems. *J Nucl Mater* 2011;417:176–9. doi:10.1016/J.JNUCMAT.2010.12.300.
- [40] Takaya S, Furukawa T, Müller G, Heinzl A, Jianu A, Weisenburger A, Aoto K, Inoue M, Okuda T, Abe F, Ohnuki S, Fujisawa T, Kimura A. Al-containing ODS steels with improved corrosion resistance to liquid lead–bismuth. *J Nucl Mater* 2012;428:125–30. doi:10.1016/J.JNUCMAT.2011.06.046.
- [41] Prorior Serre I, Vogt JB. Mechanical behavior in liquid lead of Al₂O₃ coated 15-15Ti steel and an Alumina-Forming Austenitic steel designed to mitigate their corrosion. *Eng Fail Anal* 2022;139:106443. doi:10.1016/J.ENGFANAL.2022.106443.
- [42] Li Y, Shen J, Li F, Yang H, Kano S, Matsukawa Y, Satoh Y, Fu H, Abe H, Muroga T. Effects of fabrication processing on the microstructure and mechanical properties of oxide dispersion strengthening steels. *Mater Sci Eng A* 2016;654:203–12. doi:10.1016/J.MSEA.2015.12.032.
- [43] Dash MK, Mythili R, Ravi R, Sakthivel T, Dasgupta A, Saroja S, Bakshi SR. Microstructure and mechanical properties of oxide dispersion strengthened 18Cr-ferritic steel consolidated by spark plasma sintering. *Mater Sci Eng A* 2018;736:137–47. doi:10.1016/J.MSEA.2018.08.093.
- [44] Boulnat X, Perez M, Fabregue D, Douillard T, Mathon MH, De Carlan Y. Microstructure evolution in nano-reinforced ferritic steel processed by mechanical alloying and spark plasma sintering. *Metall Mater Trans A Phys Metall Mater Sci* 2014;45:1485–97. doi:10.1007/s11661-013-2107-y.
- [45] Heintze C, Bergner F, Hernández-Mayoral M, Kögler R, Müller G, Ulbricht A. Irradiation hardening of Fe–9Cr-based alloys and ODS Eurofer: Effect of helium implantation and iron-ion irradiation at 300 °C including sequence effects. *J Nucl Mater* 2016;470:258–67. doi:10.1016/J.JNUCMAT.2015.12.041.
- [46] Lu C, Lu Z, Wang X, Xie R, Li Z, Higgins M, Liu C, Gao F, Wang L. Enhanced Radiation-tolerant Oxide Dispersion Strengthened Steel and its Microstructure Evolution under Helium-implantation and Heavy-ion Irradiation. *Sci Reports* 2017;7:1–7. doi:10.1038/srep40343.
- [47] Gong M, Zhou Z, Hu H, Zhang G, Li S, Wang M. Effects of aluminum on microstructure and mechanical behavior of 14Cr–ODS steels. *J Nucl Mater* 2015;462:502–7. doi:10.1016/J.JNUCMAT.2014.12.079.
- [48] Oh SR, Kano S, Yang H, McGrady J, Abe H. Radiation-induced nanoparticle growth in 12Cr-ODS steel at elevated temperature. *J Nucl Mater* 2020;538:152192. doi:10.1016/J.JNUCMAT.2020.152192.

- [49] Hong KH, Seol JB, Kim JH. First principles determination of formation of a Cr shell on the interface between Y–Ti–O nanoparticles and a ferritic steel matrix. *Appl Surf Sci* 2019;481:69–74. doi:10.1016/J.APSUSC.2019.03.081.
- [50] Larson DJ, Maziasz PJ, Kim IS, Miyahara K. Three-dimensional atom probe observation of nanoscale titanium-oxygen clustering in an oxide-dispersion-strengthened Fe-12Cr-3W-0.4Ti + Y₂O₃ ferritic alloy. *Scr Mater* 2001;44:359–64. doi:10.1016/S1359-6462(00)00593-5.
- [51] Odette GR. On the status and prospects for nanostructured ferritic alloys for nuclear fission and fusion application with emphasis on the underlying science. *Scr Mater* 2018;143:142–8. doi:10.1016/J.SCRIPTAMAT.2017.06.021.
- [52] Lopez J, Cerne R, Ho D, Madigan D, Shen Q, Yang B, Corpus J, Jarosinski W, Wang H, Zhang X. In Situ Reactive Formation of Mixed Oxides in Additively Manufactured Cobalt Alloy. *Materials (Basel)* 2023;16:3707. doi:10.3390/MA16103707.
- [53] Smith TM, Kantzos CA, Zarkevich NA, Harder BJ, Heczko M, Gradl PR, Thompson AC, Mills MJ, Gabb TP, Lawson JW. A 3D printable alloy designed for extreme environments. *Nature* 2023;617:513–8. doi:10.1038/s41586-023-05893-0.
- [54] Auger MA, De Castro V, Leguey T, Muñoz A, Pareja R. Microstructure and mechanical behavior of ODS and non-ODS Fe–14Cr model alloys produced by spark plasma sintering. *J Nucl Mater* 2013;436:68–75. doi:10.1016/J.JNUCMAT.2013.01.331.
- [55] Auger MA, De Castro V, Leguey T, Tarcísio-Costa J, Monge MA, Muñoz A, Pareja R. Effect of yttrium addition on the microstructure and mechanical properties of ODS RAF steels. *J Nucl Mater* 2014;455:600–4. doi:10.1016/J.JNUCMAT.2014.08.040.
- [56] Kurpaska L, Jozwik I, Lewandowska M, Jagielski J. The effect of Ar-ion irradiation on nanomechanical and structural properties of ODS RAF steels manufactured by using HIP technique. *Vacuum* 2017;145:144–52. doi:10.1016/J.VACUUM.2017.08.039.
- [57] Grobner PJ. The 885° f (475° c) embrittlement of ferritic stainless steels. *Metall Trans* 1973;4:251–60. doi:10.1007/BF02649625/METRICS.
- [58] Sang W, Dou P, Kimura A. Early-stage thermal ageing behavior of 12Cr, 12Cr–7Al and 18Cr–9Al ODS steels. *J Nucl Mater* 2020;535:152164. doi:10.1016/J.JNUCMAT.2020.152164.
- [59] Jang KN, Kim TK, Kim KT. The effect of cooling rates on carbide precipitate and microstructure of 9Cr-1Mo oxide dispersion strengthened(ODS) steel. *Nucl Eng Technol* 2019;51:249–56. doi:10.1016/J.NET.2018.09.021.
- [60] Gong J, Li Y. Energy-balance analysis for the size effect in low-load hardness testing. *J Mater Sci* 2000;35:209–13. doi:10.1023/A:1004777607553.